

Role of Particle Size in Nanocrystalline TiO₂-Based Photocatalysts

Zhibo Zhang,[†] Chen-Chi Wang,[‡] Rama Zakaria,[‡] and Jackie Y. Ying^{*,‡}

Department of Physics and Department of Chemical Engineering, Massachusetts Institute of Technology, Cambridge, Massachusetts 02139-4307

Received: July 8, 1998

This paper presents a systematic study on the role of particle size in pure and doped nanocrystalline TiO₂ photocatalysts, which was made possible by a versatile wet-chemical process capable of generating near-agglomeration-free TiO₂ with well-controlled particle sizes and dopant dispersion. It is shown that particle size is a crucial factor in the dynamics of the electron/hole recombination process. For TiO₂ particles with 6 or 11 nm diameter, Fe³⁺ dopants were added to inhibit the charge carrier surface recombination. The optimal Fe³⁺ dopant concentration for different particle sizes was identified, and this concentration was found to decrease with increasing particle size. To assist electron and hole separation in TiO₂ with 21 nm diameter, Nb⁵⁺ dopants were introduced in combination with minor surface Pt dispersion. These carefully engineered nanocrystalline TiO₂ catalysts showed higher reactivities than Degussa P25 TiO₂ material in photocatalytic decomposition of chloroform.

Introduction

Photocatalysis is an attractive low-temperature, nonenergy-intensive approach for chemical waste remediation. TiO₂ is the most investigated photocatalyst system and has been found to be capable of decomposing a wide variety of organics and inorganics in both liquid phase^{1–11} and gas phase.^{12–18} The basic principle of semiconductor photocatalysis involves photon-generated electrons (e⁻) and holes (h⁺) migrating to the surface and serving as redox sources that react with adsorbed reactants, leading to the destruction of pollutants. The current bottleneck in photocatalysis lies in its low quantum yield, which depends on the ratio of the surface charge carrier transfer rate to the electron–hole (e⁻/h⁺) recombination rate.

Particle size is an important parameter for catalysis in general since it directly impacts the specific surface area of a catalyst. With a smaller particle size, the number of active surface sites increases, and so does the surface charge carrier transfer rate in photocatalysis. However, our previous study revealed that the photocatalytic efficiency does not monotonically increase with decreasing particle size, and there exists an optimal particle size of about 10 nm for pure nanocrystalline TiO₂ photocatalyst in the liquid-phase decomposition of chloroform.¹⁹ This phenomenon is attributed to the increased surface e⁻/h⁺ recombination rate, which offsets the benefits from the ultrahigh surface area of nanocrystalline TiO₂; a detailed discussion for such effects is presented in this paper.

To increase the quantum yield of nanocrystalline photocatalysts, the e⁻/h⁺ recombination has to be reduced. An effective method to achieve the separation of e⁻ and h⁺ is to introduce defects into TiO₂ lattice through selective metal ion doping. Many transition metal ion dopants have been investigated previously for the TiO₂ system, among which Fe³⁺ has been most widely examined.²⁰ For instance, a small amount (0.2–1.0 at. %) of Fe³⁺ doping has been shown to enhance the

efficiency of photocatalytic reduction of N₂²¹ and CCl₄²² and oxidation of toluene,²³ nitrite,²⁴ and CHCl₃.²² However, Fe³⁺ doping was found to have little effect or to be detrimental for the photocatalytic oxidation of phenol²⁵ and 4-nitrophenol.²⁶ Although it has been known that the effect of Fe³⁺ doping depends on the dopant concentration, it has not been recognized that the optimal dopant concentration is strongly dependent on the particle size of the TiO₂ catalyst, which will be demonstrated in this paper.

The dominant e⁻/h⁺ recombination pathway may be different for TiO₂ of different particle size regimes,²⁷ consequently it is critical that different strategies be established for improving the photocatalytic efficiencies of different systems. In this paper, we present studies on the role of particle size in both pure and doped nanocrystalline TiO₂ photocatalysts. Since the nature of TiO₂ particle surface also plays an important role in determining the overall photocatalytic efficiency,^{28,29} in order to examine the effects of TiO₂ particle size on photocatalytic efficiency, it is important to prepare all TiO₂ catalysts with comparable surface characteristics. A versatile wet-chemical process, which allows the preparation of essentially agglomeration-free nanocrystalline TiO₂ powders with controlled particle sizes and dopant dispersions, enables this systematic investigation. Specifically, we conducted detailed studies on Fe³⁺ doping in TiO₂, and identified the optimal dopant concentration for 6 and 11 nm-sized particles. For TiO₂ with larger particle size (e.g. 21 nm), a different approach using Nb⁵⁺ doping combined with Pt dispersion is shown to be more effective toward promoting the photocatalytic efficiency. The reactivities of the various nanocrystalline systems were characterized for the liquid-phase photocatalytic decomposition of CHCl₃, and compared to that of the commercially available Degussa P25 TiO₂ material.

Experimental Section

Sample Preparation and Characterization. Nanocrystalline TiO₂ samples were prepared through sol–gel hydrolysis precipitation of titanium isopropoxide (Ti(OCH(CH₃)₂)₄), followed by hydrothermal treatment or post-calcination.¹⁹ First, 9 mL of

* To whom correspondence should be addressed.

[†] Department of Physics.

[‡] Department of Chemical Engineering.

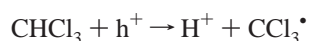
Ti(OCH(CH₃)₂)₄ (Alfa AESAR, 97%) dissolved in 41 mL of anhydrous ethanol was added dropwise to a mixed solution of 50 mL of deionized water and 50 mL of ethanol under vigorous stirring at room temperature. The as-precipitated gel was amorphous. In the hydrothermal treatment route, the gel suspension was directly transferred into high-pressure tubes and subjected to crystallization at 80 °C for 24 h or 180 °C for 96 h. The nanocrystalline TiO₂ samples thus obtained were labeled as HA and HB, respectively. The hydrothermally treated suspension was then centrifuged for powder separation, washed several times with ethanol (to minimize agglomeration by breaking hydrogen bonding between particles), and dried at room temperature. In the post-calcination route, the gel precipitate was separated from the sol, washed with ethanol, and dried overnight at 110 °C. Crystallization was achieved by calcination of the amorphous gel precipitate at 450 °C for 2 h in flowing O₂. The powder derived in this way was labeled as SA.

The above procedures were modified to incorporate dopants into TiO₂ matrix. Fe³⁺ dopants were introduced by adding an appropriate amount of Fe(NO₃)₃·9H₂O to the deionized water prior to the hydrolysis of Ti(OCH(CH₃)₂)₄. The Fe³⁺ dopant concentration was controlled to be between 0.02 and 1.0 at. %. Nb⁵⁺ dopants were introduced by co-dissolving niobium ethoxide (Alfa AESAR, 99.999%) with Ti(OCH(CH₃)₂)₄ in ethanol, and the Nb⁵⁺ dopant level was varied between 0.1 and 1.0 at. %. The dopant concentrations described in this work represented the nominal dopant quantity introduced. Since both Fe³⁺ and Nb⁵⁺ have an ionic radius similar to Ti⁴⁺, they can be easily incorporated into the TiO₂ matrix by substituting for the Ti⁴⁺ lattice sites. The solubility of Fe³⁺ in TiO₂ has been found to be as high as 1.0–1.2 at. %, ³⁰ without high-temperature treatment. The color of Fe³⁺-doped samples was yellowish while that of the Nb⁵⁺-doped samples was light blue; these colors corresponded to color centers introduced by the different transition metal ion dopants.

The Pt metal dispersion on TiO₂ particle surface was achieved by the room-temperature photodeposition of H₂PtCl₆.³¹ First, 1 g of TiO₂ powder was suspended ultrasonically in 200 mL of aqueous solution containing the desired amount of H₂PtCl₆ (Aldrich, 8 wt % in water) and 4 mL of methanol as the reducing agent for holes. The well-dispersed suspension was irradiated by a 200-W medium-pressure Mercury lamp for 4 h in an immersion-type batch reactor.¹⁹ It was then centrifuged and washed with deionized water repeatedly, and dried at room temperature, yielding a grayish Pt/TiO₂ powder.

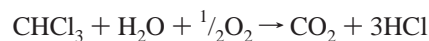
The crystalline phases of the TiO₂ powders were examined in X-ray diffraction (XRD) studies using a Siemens D5000 θ – θ diffractometer. The average grain sizes were calculated from the XRD peak broadening using Scherrer's equation. Transmission electron microscopy (TEM) studies were carried out on a JEOL 200CX or a Topcon 002B microscope operating at 200 kV. Nitrogen adsorption was employed to characterize the surface area of the powders using a Micromeritics ASAP 2000 analyzer. X-ray photoelectron spectroscopy (XPS) was utilized to verify the presence of metallic Pt deposits on TiO₂; a Surface Science Laboratory SSX-100 spectrometer with monochromatic Al K α was employed.

Photoreactivity Measurement. Photocatalytic reactivity of each sample was quantified in terms of oxidation of CHCl₃ by holes in the liquid phase,³²



where h⁺ referred to a surface-trapped hole or a surface-bound

•OH radical. CCl₃• produced 3 Cl[–] and CO₂ in the presence of O₂ and H₂O. The overall reaction stoichiometry could be expressed as



We used this reaction to quantify the photoreactivity since it does not have any intermediate product, allowing the overall photonic efficiency³³ to be easily determined. This reaction was also selected because the decomposition of halogenated organics is of great interest to groundwater purification, and because oxidation by holes represents the mechanism by which most hazardous organic compounds are photocatalytically decomposed.

The photocatalytic decomposition of CHCl₃ was carried out using a projection-type batch reactor. The irradiation was provided by a 1000-W xenon arc lamp that was hosted in an Oriel lamp housing. The light was collimated by a fused silica condenser lens, and was passed through a 7.5-cm thick Ni–Co sulfate liquid filter to absorb infrared and most of the other unwanted photons. The wavelength selection was achieved with an Oriel interference band-pass filter (310–330 nm). The light intensity could be adjusted through neutral density filters. The UV light with the desired intensity and wavelength was then focused onto a custom-designed glass reaction cell with an optical-grade quartz window to allow transmission of UV photons. The final photon intensities were measured by chemical actinometry.³⁴ For each run, a 1.2 × 10^{–2} M CHCl₃ solution with a catalyst loading of 0.5 g/L was used as the reaction colloidal dispersion. The initial pH of the reaction medium was adjusted to 11.0 ± 0.2 with the addition of 1.0 N NaOH solution; the high pH was chosen to neutralize the H⁺ ions generated during the CHCl₃ decomposition. The reaction cell (55 mL in capacity) was then filled with the reaction medium, which was bubbled through with O₂ and constantly agitated by a magnetic stir bar during the experiment. After 30 min of irradiation, the extent of CHCl₃ decomposition was determined by measuring the Cl[–] concentration with a chloride ion selective electrode. The UV light intensity used in all experiments was 1.8 × 10^{–4} Einstein L^{–1} min^{–1}, and the photon intensity on the quartz window was 2.5 × 10¹⁷ cm^{–2} s^{–1}. Photolysis experiment in which no photocatalyst was added was also performed with otherwise exactly the same experimental conditions, and no measurable CHCl₃ decomposition was detected. The photodecomposition measurements were repeated for each catalytic system, and the experimental error was found to be within ± 5%.

Results

Material Characteristics. To study the influence of particle size on nanocrystalline TiO₂-based photocatalysts, TiO₂ samples with narrow size distribution and negligible agglomeration were required. To allow for a direct comparison of photoreactivities of TiO₂ with varying doping levels, the material characteristics, such as crystalline phase, particle size and surface area, also should not be significantly affected by the dopant concentration.

Figure 1 shows the XRD patterns of pure TiO₂ with varying grain sizes. Samples HA and HB, generated through the hydrothermal treatment, were mostly anatase with a minor brookite component. Sample SA, which was crystallized by calcination at 450 °C, has a pure anatase phase. Average grain sizes calculated from the broadening of the (101) XRD peak of anatase phase were about 6, 11, and 21 nm for samples HA,

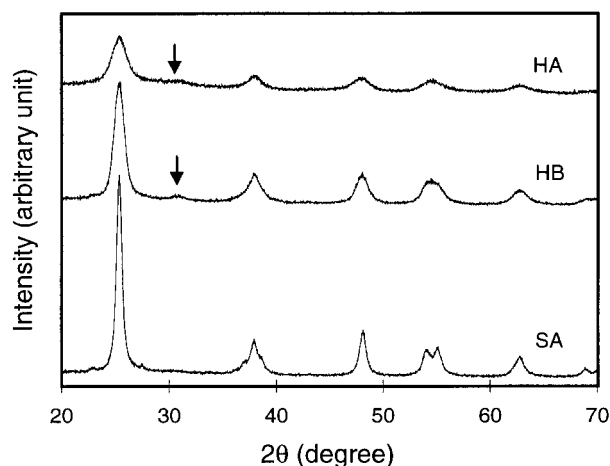


Figure 1. XRD patterns of pure TiO₂ samples with different grain sizes: (HA) 6 nm, (HB) 11 nm, and (SA) 21 nm. The peak marked with an arrow corresponds to the brookite phase, while all other peaks belong to the anatase phase.

HB, and SA, respectively. As for the samples with dopant concentrations of interest to this work (0.02–1.0 at. % for Fe³⁺ and 0.1–1.0 at. % for Nb⁵⁺), we did not observe any secondary phase, and the minor variation in particle size due to different doping levels was within the experimental uncertainty. The transmission electron micrographs, shown in Figure 2, indicate that all three samples have negligible agglomeration. The particle sizes of these three samples determined from the TEM micrographs were 6.2 ± 2.1 , 10.1 ± 2.7 , and 22.1 ± 5.5 nm, respectively (the uncertainties were represented by $2 \times$ standard deviation). We note that all three samples have a reasonably narrow particle size distribution, and the average particle sizes obtained from TEM were consistent with those calculated from the XRD peak broadening. A high-resolution electron micrograph (HREM) of sample HA is presented in Figure 2d, showing that the TiO₂ samples were well crystallized even for grains as small as 6 nm. The surface areas of samples HA, HB, and SA measured by N₂ adsorption (using the 5-point BET method) were 253, 146, and 70 m²/g, respectively; Fe³⁺ or Nb⁵⁺ doping did not change the surface area by more than $\pm 10\%$, allowing for direct comparison of the effects of the different doping levels examined. Considering the density of anatase (3.9 g/cm³), if these spherical particles were assumed to be completely free of agglomeration, the average particle sizes corresponding to the surface areas of 253, 146, and 70 m²/g would be 6.1, 10.5, and 22.0 nm, respectively. These theoretical values were well matched with the particle sizes determined by XRD peak broadening and TEM, confirming that the degree of agglomeration was negligible for all three samples prepared.

For the 0.5 wt % Pt-loaded TiO₂ samples, only the characteristic peaks corresponding to the TiO₂ anatase phase were observed in the XRD patterns, and no peaks corresponding to Pt metal were noted. The absence of Pt peaks could be attributed to their ultrahigh dispersion on TiO₂ particles as very small clusters. The BET surface area for the Pt-loaded samples was also very similar to that of the pure TiO₂. In the XPS spectra, the characteristic peak of Pt 4f_{7/2} with a binding energy of 70.3 eV was observed for the Pt-loaded samples, confirming the presence of Pt⁰ metal. XPS peaks corresponding to other possible oxidation states of Pt, such as Pt²⁺ or Pt⁴⁺, were not found. The TEM shown in Figure 3 reveals that the Pt islands were well dispersed with an average cluster size of about 2 nm on the TiO₂ particles.

Photocatalytic Studies. The results of photocatalytic degradation of CHCl₃ over nanocrystalline TiO₂ with varying particle sizes and different Fe³⁺ dopant concentrations are presented in Table 1. The Cl[−] molar concentrations ([Cl[−]]) of the reaction media measured after 30 min of UV irradiation, and the calculated photonic efficiencies are shown. In this paper, photonic efficiency³³ is defined as

$$\text{photonic efficiency} = [\text{Cl}^-]/(3It)$$

where I is the photon intensity, and t is the irradiation time; in our experiments, $I = 1.8 \times 10^{-4}$ Einstein L^{−1} min^{−1}, and $t = 30$ min. For pure TiO₂ catalyst, the sample with an average diameter of 11 nm showed the highest photonic efficiency, while the 6-nm sample showed a photoreactivity that was 26% lower. The TiO₂ sample with an average diameter of 21 nm and the lowest surface area gave the lowest photoreactivity. These results are consistent with our previous studies¹⁹ whereby the photocatalytic measurements were carried out at a much higher photon intensity ($\sim 2.0 \times 10^{-3}$ Einstein L^{−1} min^{−1}). For TiO₂ samples with an average diameter of 6 nm, a small amount of Fe³⁺ dopants significantly enhanced the photoreactivity. The highest conversion for the 6-nm TiO₂ sample was achieved at an Fe³⁺ concentration of 0.2 at. %; Fe³⁺ doping became detrimental when the dopant concentration was 0.5 at. % or higher. A similar behavior was observed in TiO₂ with an average diameter of 11 nm, but the optimal Fe³⁺ concentration was 0.05 at. %, which was lower than the optimal dopant concentration of 0.2 at. % for 6-nm TiO₂.

Table 2 presents the photocatalytic results for TiO₂ samples with different Nb⁵⁺ dopant concentrations. For both 11- and 21-nm TiO₂ samples, the photoreactivities were reduced by sole Nb⁵⁺ doping, and the photonic efficiencies decreased monotonically with increasing Nb⁵⁺ concentration for dopant concentrations of less than 1.0 at. %. Table 3 shows the effects of Pt loading combined with Nb⁵⁺ doping. For both 11- and 21-nm TiO₂ systems, a small amount (0.5 wt %) of Pt loading on TiO₂ particle surface significantly enhanced the photoreactivities. The photoreactivity of the 21-nm TiO₂ sample loaded with 0.5 wt % Pt was further increased when a small amount (0.2–0.5 at. %) of Nb⁵⁺ dopants was introduced into the TiO₂ matrix. However, when Nb⁵⁺ dopant concentration was increased to 1.0 at. %, a negative effect on photonic efficiency was noted. The optimal Nb⁵⁺ concentration for 0.5 wt % Pt-loaded 21-nm TiO₂ was found to be ~ 0.5 at. %.

In summary, of the various TiO₂-based samples investigated, 6-nm TiO₂ doped with 0.2 at. % Fe³⁺, 11-nm TiO₂ doped with 0.05 at. % Fe³⁺, and 21-nm TiO₂ doped with 0.5 at. % Nb⁵⁺ and loaded with 0.5 wt % Pt gave the best photocatalytic activity in liquid-phase CHCl₃ decomposition. To allow direct comparison of our results to the literature values, the most widely studied (and probably the best) commercially available TiO₂ catalyst, Degussa P25, was also examined for photoreactivity under the same experimental conditions. The results are presented in Figure 4; we note that our three optimized photocatalysts showed comparable reactivities, and all were more active than Degussa P25. The photonic efficiency of Degussa P25 obtained in our experiment (2.9%) is somewhat lower than the literature value (4.0%³²) for CHCl₃ decomposition, this discrepancy might be due to the systematic difference resulted from different experimental setups used by different groups. However, this systematic difference should not affect the comparison of photocatalytic activities of different catalysts

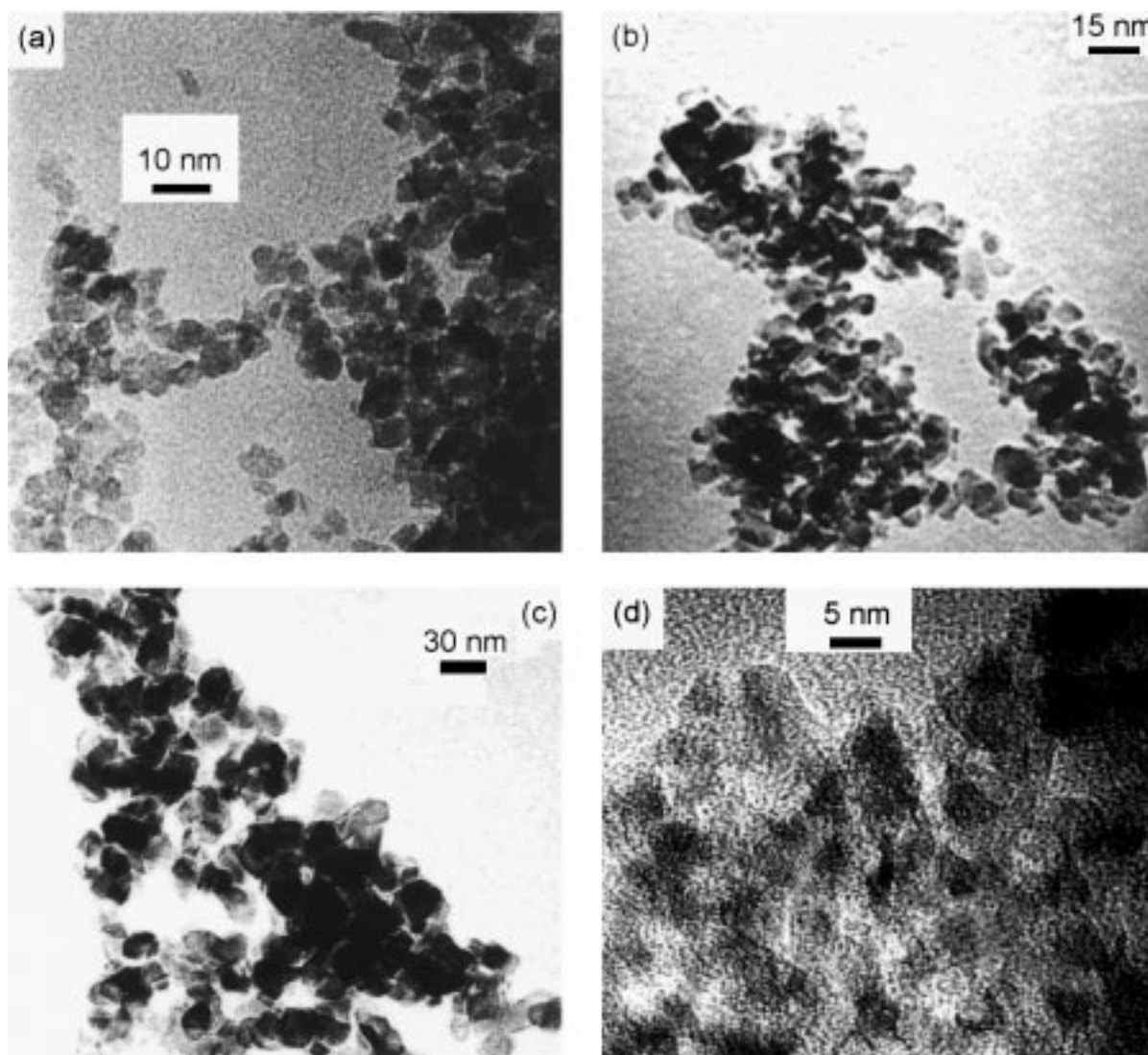


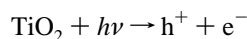
Figure 2. TEM micrographs of pure TiO₂ samples with different average particle sizes: (a) sample HA, (b) sample HB, and (c) sample SA. (d) A HREM image of sample HA, showing the lattice fringes of the 6-nm TiO₂ nanocrystallites.

determined in a consistent manner in our experiments.

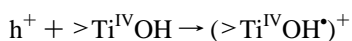
Discussions

Mechanism of Photocatalytic Processes in TiO₂. When an UV photon is absorbed by TiO₂, which is a wide band gap semiconductor, an e⁻/h⁺ pair is generated. The e⁻ and h⁺ may migrate to the surface and react with the adsorbed reactants in the desired process, or they may undergo undesired recombination. A rate increase in the former process or a rate decrease in the latter would lead to a greater photocatalytic efficiency. The primary processes in photocatalysis can be summarized as follows:¹¹

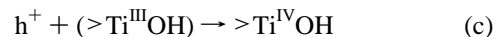
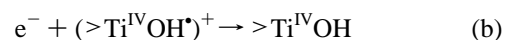
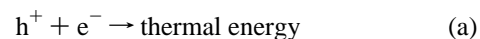
Charge carrier generation:



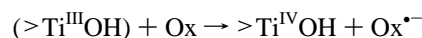
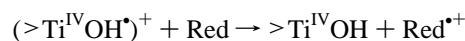
Charge carrier trapping:



Charge carrier recombination:



Interfacial charge transfer:



where $h\nu$ is an UV photon, $>\text{TiOH}$ represents the hydrated surface functional group, $(>\text{Ti}^{\text{III}}\text{OH})$ is the surface-trapped conduction band electron while $(>\text{Ti}^{\text{IV}}\text{OH}^*)^+$ is the surface-trapped valence band hole, Red is a reductant, and Ox is an oxidant. Because the characteristic times of the primary processes in photocatalysis strongly depend on material characteristics of a specific photocatalyst,^{22,28,35–37} it would be difficult to provide a generalized value for the characteristic time of each process. However, the characteristic times of the interfacial charge transfer (especially for e⁻) are usually much slower than those of the charge carrier trapping and recombination processes.

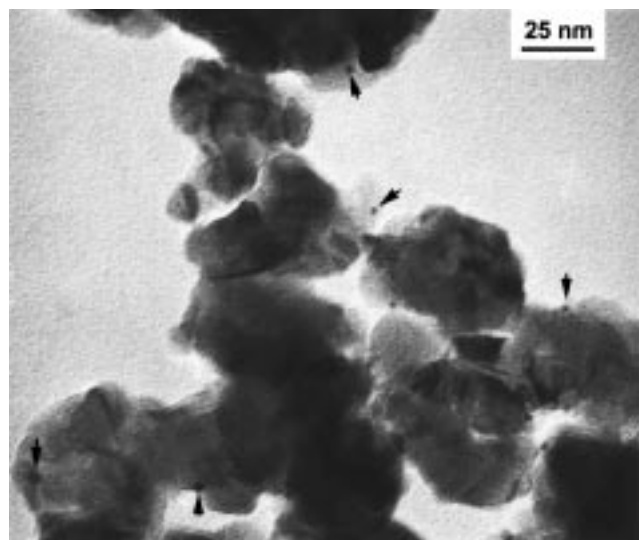


Figure 3. TEM micrograph of a 0.5 wt % Pt-loaded TiO₂ sample with an average TiO₂ particle size of 21 nm. The arrows are pointing to 2-nm Pt islands dispersed on the TiO₂ particle surface.

TABLE 1: Measured Cl⁻ Concentrations ([Cl⁻]) after 30 min of UV Irradiation and Calculated Photonic Efficiencies for the CHCl₃ Decomposition over TiO₂ Samples with Different Particle Sizes and Fe³⁺ Dopant Concentrations^a

particle size (nm)	[Cl ⁻] (mM)/Photonic Efficiency (%)					
	Fe ³⁺ dopant concentration (at. %)					
	0.0	0.02	0.05	0.1	0.2	0.5
6	0.30/1.9		0.37/2.3	0.44/2.7	0.79/4.8	0.24/1.5
11	0.42/2.6	0.48/3.0	0.80/4.9	0.53/3.3	0.43/2.7	
21	0.26/1.6					

^a The initial reaction conditions were [CHCl₃] = 12 mM and pH = 11, and the catalyst loadings were 0.5 g/L.

TABLE 2: Measured Cl⁻ Concentrations ([Cl⁻]) after 30 min of UV Irradiation and Calculated Photonic Efficiencies for CHCl₃ Decomposition over 11- and 21-nm TiO₂ Samples with Different Nb⁵⁺ Dopant Concentrations^a

particle size (nm)	[Cl ⁻] (mM)/Photonic Efficiency (%)				
	Nb ⁵⁺ dopant concentration (at. %)				
	0.0	0.1	0.2	0.5	1.0
11	0.42/2.6	0.32/2.0		0.25/1.6	0.23/1.4
21	0.26/1.6		0.24/1.5	0.23/1.4	

^a The initial reaction conditions were [CHCl₃] = 12 mM and pH = 11, and catalyst loadings were 0.5 g/L.

TABLE 3: Measured Cl⁻ Concentrations ([Cl⁻]) after 30 min of UV Irradiation and Calculated Photonic Efficiencies for CHCl₃ Decomposition over Pure or 0.5 wt % Pt-Loaded 11- and 21-nm TiO₂ Samples with Different Nb⁵⁺ Dopant Concentrations^a

particle size (nm)	[Cl ⁻] (mM)/Photonic Efficiency (%)				
	Pt loading (wt %)/Nb ⁵⁺ dopant concentration (at. %)				
	0.0/0.0	0.5/0.0	0.5/0.2	0.5/0.5	0.5/1.0
11	0.42/2.6	0.67/4.1			
21	0.26/1.6	0.59/3.6	0.64/3.9	0.79/4.8	0.52/3.2

^a The initial reaction conditions were [CHCl₃] = 12 mM and pH = 11, and the catalyst loadings were 0.5 g/L.

Particle Size Effect in Pure TiO₂. For pure TiO₂, the e⁻/h⁺ recombination may be grouped into two categories: volume recombination (a) and surface recombination (b and c). Volume

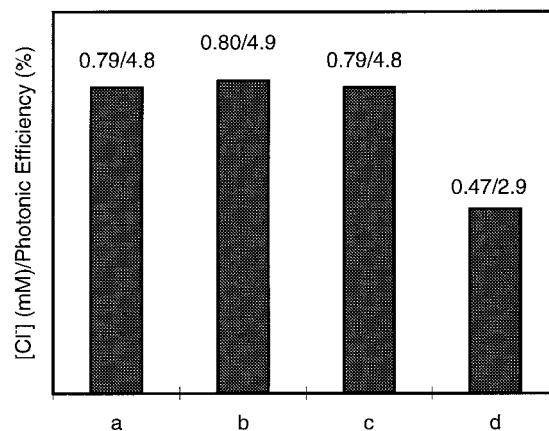


Figure 4. Measured Cl⁻ concentrations ([Cl⁻]) after 30 min of UV irradiation and the calculated photonic efficiencies for CHCl₃ decomposition over various photocatalysts: (a) 0.2 at. % Fe³⁺-doped 6-nm TiO₂, (b) 0.05 at. % Fe³⁺-doped 11-nm TiO₂, (c) 0.5 at. % Nb⁵⁺-doped 21-nm TiO₂ with 0.5 wt % Pt loading, and (d) Degussa P25 TiO₂. The initial reaction conditions were: [CHCl₃] = 12 mM and pH = 11, and the catalyst loadings were 0.5 g/L. The thickness of the reaction media was about 2.5 cm, which guaranteed that all the incident UV photons were absorbed by TiO₂.

recombination is a dominant process in well-crystallized large TiO₂ particles,²⁷ which can be reduced by decreasing particle size. Reduction in particle size also leads to larger surface area, which increases the available surface active sites. A decrease in particle size should also lead to a higher photonic efficiency from a higher interfacial charge carrier transfer rate. However, in nanocrystalline semiconductor particles, when particle size becomes extremely small (i.e. several nm in diameter), surface recombination becomes an important process.^{27,38} In the regime of ultrafine particle size, most of the e⁻/h⁺ pairs are generated sufficiently close to the surface. They may quickly reach the surface, and undergo rapid surface recombination mainly due to abundant surface trapping sites and the lack of driving force for e⁻/h⁺ pair separation. Since the characteristic time for surface e⁻/h⁺ recombination is much faster than that of the interfacial charge carrier transfer processes, the increase in the interfacial transfer rate will be outweighed by the increased surface recombination rate in ultrafine particles beyond a certain size reduction. Therefore, an optimal particle size exists in the pure TiO₂ system for the maximum photocatalytic efficiency. This argument is supported by our experimental results: the photo-reactivity of pure TiO₂ increases when particle size is reduced from 21 to 11 nm, but decreases when it is further reduced to 6 nm. A particle size of about 10 nm might be the optimal value for pure TiO₂ photocatalyst in liquid-phase decomposition of CHCl₃. Our photocatalytic results are also consistent with previous study on the different lifetimes of e⁻/h⁺ pairs in nanocrystalline TiO₂ particles with different particle sizes determined by transient photoabsorption spectroscopy,²⁷ whereby TiO₂ particles with a diameter of 13.3 nm was found to have a longest emission decay time.

Particle Size Effect in Fe³⁺-Doped TiO₂. To utilize the ultrahigh surface area of nanocrystalline TiO₂ particles for greater photoreactivity, we have to find a way to inhibit the surface e⁻/h⁺ recombination. A commonly practiced strategy is to introduce shallow charge trapping sites into the TiO₂ matrix, and Fe³⁺ has been shown to be one of the most effective dopants. However, the role of Fe³⁺ dopants in TiO₂ is controversial. Soria et al. suggested that Fe³⁺ served as trapping sites for both e⁻ and h⁺,^{21b} while Moser et al. postulated that Fe³⁺ only trapped h⁺ while e⁻ was trapped by surface Ti⁴⁺

site.³⁹ The lack of information on the energy levels of $\text{Fe}^{2+/3+}$ and $\text{Fe}^{3+/4+}$ in anatase makes it difficult to tell which hypothesis is correct.

However, regardless of which of these postulates is true, we would expect that an optimal Fe^{3+} dopant concentration exists and that it should strongly depend on the particle size of TiO_2 . As discussed above, it has been accepted that Fe^{3+} doping increases the photocatalytic efficiency as Fe^{3+} serves as shallow trapping sites for the charge carriers, thereby separating the arrival time of e^- and h^+ at the surface. The best effect would be achieved if one charge carrier of the e^-/h^+ pair is temporarily trapped while the other migrates to the surface first and transfers to the adsorbate (oxidant for e^- and reductant for h^+), with the trapped charge carrier migrating to the surface soon afterward for reaction as well. Here, shallow trapping is critical,²² which means that the trapped charge carrier can be thermally excited from the trapping site and becomes mobile again, preferably before the generation of the next e^-/h^+ pair inside the same particle. A deeply trapped charge carrier will recombine with its counterpart generated by a subsequent photon so that its overall effect is serving as a charge carrier recombination center, which is detrimental to the overall photocatalytic efficiency. However, even for the shallow trapping sites introduced by dopants such as Fe^{3+} , a high doping concentration is not desirable. This argument should apply regardless if Fe^{3+} serves as trapping site for both e^- and h^+ or for h^+ only. If the first case is true, then at a high dopant concentration, the possibility that both charge carriers of the e^-/h^+ pair are trapped will be high, and this trapped charge carrier pair may recombine through quantum tunneling.⁴⁰ If the Fe^{3+} dopant can only trap h^+ , then the recombination through trapped e^-/h^+ pair may not be as great a concern. However, at a high dopant concentration, a h^+ may be trapped more than once on its way to the surface so that its apparent mobility may become extremely low and it will likely recombine with e^- generated by subsequent photons before it can reach the surface. Thus, an optimal Fe^{3+} dopant concentration should be expected to exist in either case; this is exactly what has been observed by various research groups,²⁰ and is also believed to be the reason that the photonic efficiency was observed to strongly depend on the Fe^{3+} dopant concentration in our experiments (as shown in Table 1).

Although the observation that an optimal Fe^{3+} dopant concentration exists is not new, we can extend the hypothesis further based on this study that the optimal Fe^{3+} dopant concentration should decrease with increasing TiO_2 particle size. As we have discussed in the paragraph above, ideally only one charge carrier of the e^-/h^+ pair should be trapped by Fe^{3+} , and it is preferably trapped only once before it reaches the surface. When particle size becomes larger, the average path length of a charge carrier to the surface is longer. If the dopant concentration does not change, the possibility that a charge carrier meets a dopant increases, and so does the chance of multiple trappings. To reduce the possibility of multiple trappings, the dopant concentration should be decreased with a increasing particle size. Our experimental results support this argument. As shown in Table 1, the optimal Fe^{3+} concentration decreases from 0.2 at. % for the 6-nm TiO_2 to 0.05 at. % for the 11-nm sample.

Since the optimal Fe^{3+} concentration is expected to be even smaller in 21-nm TiO_2 , the accuracy of a very low dopant concentration (<0.01 at. %) becomes difficult to control in the wet-chemical process that was used in this study. Due to this reason, we did not conduct the investigation of Fe^{3+} doping on TiO_2 particles >11 nm. However, there are two results in the

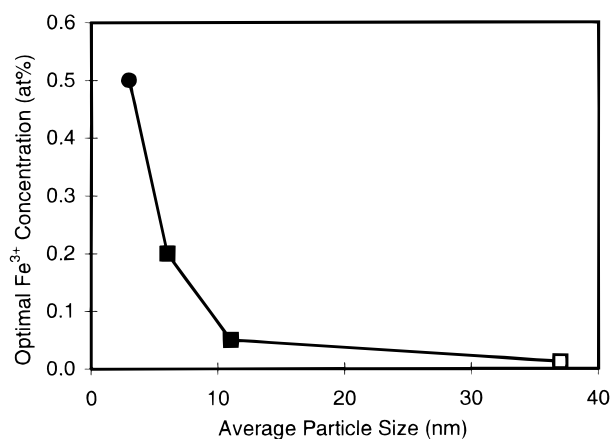


Figure 5. Optimal Fe^{3+} dopant concentrations for TiO_2 of different average particle sizes, where ● and ■ represent the results established in Choi et al.'s study²² and this study, respectively, and □ represents Fe^{3+} concentration found in Degussa P25 TiO_2 .

literature that we would like to mention, and they are consistent with our findings. The first one is Choi et al.'s study,²² which was carried out under photocatalytic conditions similar to ours, and they found that the optimal Fe^{3+} concentration is 0.5 at. % for TiO_2 with a particle size of 2–4 nm. Another observation is the Fe^{3+} impurity concentration in Degussa P25, which is about 120 ppm, or 0.012 at. %.⁴¹ Degussa P25 consists of about 80% anatase and 20% rutile, and its primary particle size is about 30 nm.⁴² Although some researchers suggested that the mixed phase of anatase and rutile was responsible for Degussa P25's high photocatalytic reactivity,⁴³ our TEM and XRD results (see Appendix A) do not support such an argument. Here we propose a different explanation, that the high photoreactivity of Degussa P25 is due to its high crystallinity and a minor Fe^{3+} doping, and the photoreactivity of Degussa P25 is mainly derived from its anatase phase. The optimal Fe^{3+} dopant concentration for a broad range of TiO_2 particle sizes is presented in Figure 5, which clearly supports our argument that the optimal Fe^{3+} concentration decreases with increasing particle size. This finding may be used to explain some of the controversial results reported in previous investigations on Fe^{3+} doping,^{25,26} where the detrimental effects observed might be due to the relatively high Fe^{3+} doping levels (0.5–1 at. %) applied to the large TiO_2 particles examined (>25 nm, estimated from the reported surface areas of the TiO_2 catalysts).

Strategy for Improving Photocatalytic Efficiency of TiO_2 with Large Particle Size. As discussed earlier, the Fe^{3+} doping should work less effectively for TiO_2 with large particle size since the dominant charge carrier recombination process in large particles is volume recombination instead of surface recombination, due to their lower surface areas. For TiO_2 in the particle size range above 10 nm, a different strategy may be used to assist the charge carrier separation. This strategy involves doping TiO_2 with cations of higher valence than Ti^{4+} (such as Nb^{5+} , Ta^{5+} , and W^{6+}) to enhance the surface band bending associated with the space charge layer, in combination with Pt cluster dispersion on the TiO_2 particle surface. This approach has been shown to be effective in increasing the photocatalytic efficiency of water cleavage,^{44,45} and recently Pt/ TiO_2 catalyst has been examined for photocatalytic degradation of organic chemicals.^{16,46} The mechanism of Pt/ TiO_2 photocatalysis involves the nature of the semiconductor–liquid interface, and has been the subject of several books and review papers.^{40,47}

Although pure TiO_2 is a natural n-type semiconductor, the small conduction e^- concentration is not enough to generate a

substantial surface band bending⁴⁷ for effective e⁻/h⁺ pair separation⁴⁸ in undoped nanocrystalline TiO₂ particles. The surface band bending could be enhanced by Nb⁵⁺ doping, however, under steady irradiation, the surface band bending will be reduced due to the accumulation of e⁻ inside the TiO₂ particle. Furthermore, the accumulated e⁻ may serve as recombination center for h⁺ generated by subsequent photons, thereby leading to a lower photonic efficiency than that of the undoped TiO₂. This is illustrated by our experimental results shown in Table 2.

Loading small Pt islands onto TiO₂ particles may prevent the e⁻ accumulation by providing a fast pathway for e⁻ interfacial transfer. Several methods have been reported for Pt dispersion onto TiO₂ particles, of which the photodeposition used in this work was found to be one of the favorable routes for generating efficient Pt/TiO₂ photocatalyst.^{44,49} Although it is still controversial as to whether the Pt–TiO₂ interface forms an ohmic contact⁵⁰ or a Schottky barrier,⁴⁵ a small amount of Pt dispersion on undoped TiO₂ particles can enhance the photocatalytic efficiencies due to the shorter characteristic time for e⁻ interfacial transfer from Pt island than that from the TiO₂ surface trapping sites. When Pt dispersion is combined with Nb⁵⁺ doping of TiO₂, the enhanced surface band bending resulted from Nb⁵⁺ doping can be utilized for e⁻/h⁺ pair separation to further enhance the photocatalytic efficiency.^{44,45} However, when Nb⁵⁺ dopant concentration is too high, the band bending may only occur in a thin layer near the surface, so that most of the particle interior will be lacking in potential drop, making the overall band bending strategy less effective.⁴⁵ These reasonings may explain the experimental results presented in Table 3.

Further Improvement of the Photocatalyst Design. In Figure 4, we compared our best photocatalysts with the industrial standard, Degussa P25. It is surprising to note that our best three photocatalysts achieved very similar photonic efficiencies. This might be a coincidence, or might be due to some unknown factors limiting the photonic efficiency in our experiment. We note that although the Nb⁵⁺-doped 21-nm TiO₂ with Pt loading provides a comparable photonic efficiency as the Fe³⁺-doped 11- and 6-nm catalysts, the high cost of Pt will likely make the former less attractive for commercial applications.

The nanocrystalline TiO₂ catalysts in our study were synthesized by a wet-chemical route. Such low-temperature processing may not be ideal for producing fully crystallized TiO₂. The photoreactivity of the Fe³⁺-doped TiO₂ of 6- or 11-nm particle sizes will likely be further increased if a synthesis route, such as the flame process for producing Degussa P25, is developed for producing ultrafine TiO₂ with controlled Fe³⁺ doping since the high temperature in gas-phase synthesis can lead to greater crystallinity in the samples generated.

Conclusions

In this paper, we have shown that particle size plays an important role in nanocrystalline TiO₂-based photocatalysts mostly through influencing the dynamics of e⁻/h⁺ recombination. We found that doping TiO₂ of diameters ≤11 nm with Fe³⁺ may improve photonic efficiency by inhibiting surface e⁻/h⁺ recombination. However, its effectiveness depends on the dopant concentration, and the optimal Fe³⁺ doping level is governed by the particle size of TiO₂. Through quantitative analysis of photonic efficiency in photocatalytic decomposition of CHCl₃, the optimal Fe³⁺ concentrations were established for different TiO₂ particle sizes and were found to decrease with increasing particle sizes. We demonstrated that by carefully

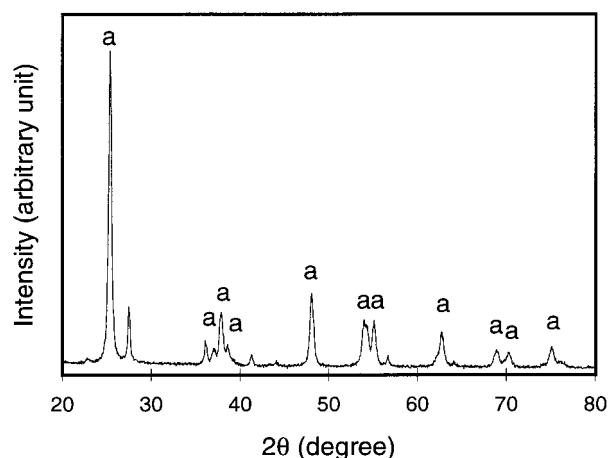


Figure A1. XRD pattern of Degussa P25. Peaks of anatase phase are marked, while all other peaks belong to the rutile phase.

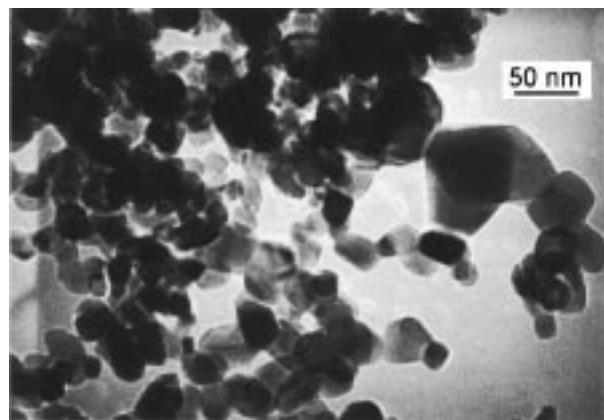


Figure A2. TEM micrograph of Degussa P25. The small particles are believed to be anatase, while the large particles are rutile.

controlling dopant concentration and minimizing particle agglomeration, Fe³⁺-doped TiO₂ of ≤11 nm could show greater photoreactivity than Degussa P25. For TiO₂ with intermediate particle size (~20 nm), we confirmed that the strategy of using enhanced surface band bending to assist e⁻/h⁺ separation works only if it is combined with Pt loading on the TiO₂ particle surface.

Acknowledgment. This project is supported by the INEEL University Research Consortium and the National Science Foundation (DMR-9400334). We thank H. Huang (MIT Department of Chemical Engineering) for his technical assistance and M. Frongillo (MIT CMSE) for his help in the TEM experiments.

Appendix A: Physical Properties of Degussa P25.

Shown in Figure A1 is the XRD pattern of Degussa P25. This TiO₂ material consists mainly of anatase with a minor component of rutile. From the broadening of the (101) peak of anatase and the (110) peak of rutile, the average grain size of each phase was calculated with Scherrer's formula to be 37 and 90 nm, respectively. These values agree with the results from TEM experiments (Figure A2). We note from the micrograph that the majority of the anatase grains (the small particles) is not in contact with the rutile grains (the big particles), so it is questionable that the anatase/rutile phase interactions play a significant role in promoting the charge carrier separation. Since the rutile in Degussa P25 has a very large particle size (~90 nm), its surface area and photoreactivity should be very low.

Therefore, we believe the high photoreactivity of Degussa P25 should be mainly attributed to the anatase phase.

References and Notes

- (1) Alekabi, H.; Serpone, N. *J. Phys. Chem.* **1988**, *92*, 5726.
- (2) Martin, S. T.; Lee, A. T.; Hoffmann, M. R. *Environ. Sci. Technol.* **1995**, *29*, 2567.
- (3) Choi, W. Y.; Hoffmann, M. R. *Environ. Sci. Technol.* **1997**, *31*, 89.
- (4) Prairie, M. R.; Evans, L. R.; Stange, B. M.; Martinez, S. L. *Environ. Sci. Technol.* **1993**, *27*, 1776.
- (5) Stafford, U.; Gray, K. A.; Kamat, P. V. *J. Phys. Chem.* **1994**, *98*, 6343.
- (6) Vinodgopal, K.; Wynkoop, D. E.; Kamat, P. V. *Environ. Sci. Technol.* **1996**, *30*, 1660.
- (7) Schmelling, D. C.; Gray, K. A.; Kamat, P. V. *Environ. Sci. Technol.* **1996**, *30*, 2547.
- (8) Huang, M.; Tso, E.; Datye, A. K.; Prairie, M. R.; Stange, B. M. *Environ. Sci. Technol.* **1996**, *30*, 3084.
- (9) Madden, T. H.; Datye, A. K.; Fulton, M.; Prairie, M. R.; Majumdar, S. A.; Stange, B. M. *Environ. Sci. Technol.* **1997**, *31*, 3475.
- (10) Sun, L. Z.; Bolton, J. R. *J. Phys. Chem.* **1996**, *100*, 4127.
- (11) Hoffmann, M. R.; Martin, S. T.; Choi, W.; Bahnemann, D. W. *Chem. Rev.* **1995**, *95*, 69 and references therein.
- (12) Nimlos, M. R.; Jacoby, W. A.; Blake, D. M.; Milne, T. A. *Environ. Sci. Technol.* **1993**, *27*, 732.
- (13) Jacoby, W. A.; Nimlos, M. R.; Blake, D. M.; Noble, R. D.; Koval, C. A. *Environ. Sci. Technol.* **1994**, *28*, 1661.
- (14) Grela, M. A.; Colussi, A. J. *J. Phys. Chem.* **1996**, *100*, 10150.
- (15) Muggli, D. S.; Larson, S. A.; Falconer, J. L. *J. Phys. Chem.* **1996**, *100*, 15886.
- (16) Sadeghi, M.; Liu, W.; Zhang, T. G.; Stavropoulos, P.; Levy, B. J. *Phys. Chem.* **1996**, *100*, 19466.
- (17) Ohko, Y.; Tryk, D. A.; Hashimoto, K.; Fujishima, A. *J. Phys. Chem. B* **1998**, *102*, 2699.
- (18) Obee, T. N.; Brown, R. T. *Environ. Sci. Technol.* **1995**, *29*, 1223.
- (19) Wang, C.-C.; Zhang, Z.; Ying, J. Y. *Nanostr. Mater.* **1997**, *9*, 583.
- (20) Litter, M. I.; Navio, J. A. *J. Photochem. Photobiol. A* **1996**, *98*, 171.
- (21) (a) Schrauzer, G. N.; Guth, T. D. *J. Am. Chem. Soc.* **1977**, *99*, 7189. (b) Soria, J.; Conesa, J. C.; Augugliaro, V.; Palmisano, L.; Schiavello, M.; Sclafani, A. *J. Phys. Chem.* **1991**, *95*, 274.
- (22) Choi, W.; Termin, A.; Hoffmann, M. R. *J. Phys. Chem.* **1994**, *98*, 13669.
- (23) Navio, J. A.; Garcia Gomez, M.; Pradera Adrian, M. A.; Fuentes Mota, J. In *Heterogeneous Catalysis and Fine Chemicals II*; Elsevier: Amsterdam, 1991; p 445.
- (24) Milis, A.; Peral, J.; Domenech, X. *J. Mol. Catal.* **1994**, *87*, 67.
- (25) Palmisano, L.; Augugliaro, V.; Sclafani, A.; Schiavello, M. *J. Phys. Chem.* **1988**, *92*, 6710.
- (26) Palmisano, L.; Schiavello, M.; Sclafani, A.; Martin, C.; Martin, I.; Rives, V. *Catal. Lett.* **1994**, *24*, 303.
- (27) Serpone, N.; Lawless, D.; Khairlutdinov, R.; Pelizzetti, E. *J. Phys. Chem.* **1995**, *99*, 16655.
- (28) Cerrato, G.; Marchese, L.; Morterra, C. *Appl. Surf. Sci.* **1993**, *70*, 200.
- (29) Rivera, A. P.; Tanaka, K.; Hisanaga, T. *Appl. Catal. B: Environ.* **1993**, *3*, 37.
- (30) Bickley, R. I.; Lees, J. S.; Tilley, R. J.; Palmisano, L.; Schiavello, M. *J. Chem. Soc., Faraday Trans.* **1992**, *88*, 377.
- (31) Tabata, S.; Nishida, H.; Masaki, Y.; Tabata, K. *Catal. Lett.* **1995**, *34*, 245.
- (32) Kormann, C.; Bahnemann, D. W.; Hoffmann, M. R. *Environ. Sci. Technol.* **1991**, *25*, 494.
- (33) Serpone, N.; Terzian, R.; Lawless, D.; Kennepohl, P.; Sauve, G. *J. Photochem. Photobiol. A* **1993**, *73*, 11.
- (34) Braun, A. M.; Maurette, M.-T.; Oliveros, E. *Photochemical Technology*; Ollis, D. F., Serpone, N., transl.; John Wiley & Sons: New York, 1991; p 70.
- (35) Colombo, D. P.; Bowman, R. M. *J. Phys. Chem.* **1996**, *100*, 18445.
- (36) Ohtani, B.; Bowman, R. M.; Colombo, D. P.; Kominami, H.; Noguchi, H.; Uosaki, K. *Chem. Lett.* **1998**, 579.
- (37) Behnemann, D. W.; Hilgendorff, M.; Memming, R. *J. Phys. Chem. B* **1997**, *101*, 4265.
- (38) (a) Hines, M. A.; Guyot-Sionnest, P. *J. Phys. Chem.* **1996**, *100*, 468. (b) Kortan, A. R.; Hull, R.; Opila, R. L.; Bawendi, M. G.; Steigerwald, M. L.; Carroll, P. J.; Brus, L. E. *J. Am. Chem. Soc.* **1990**, *112*, 1327.
- (39) Moser, J.; Grätzel, M.; Gallay, R. *Helv. Chim. Acta* **1987**, *70*, 1596.
- (40) Grätzel, M. *Photocatalysis: Fundamentals and Applications*; John Wiley & Sons: New York, 1989; p 123.
- (41) Material data sheet of Degussa P25.
- (42) Tahiri, H.; Serpone, N.; van Mao, R. L. *J. Photochem. Photobiol. A* **1996**, *93*, 199.
- (43) Bickley, R. I.; Gonzales-Carreno, T.; Lees, J. S.; Palmisano, L.; Tilley, R. J. D. *J. Solid State Chem.* **1991**, *92*, 178.
- (44) Borgarello, E.; Kiwi, J.; Pelizzetti, E.; Visca, M.; Grätzel, M. *J. Am. Chem. Soc.* **1981**, *103*, 6324.
- (45) Karakitsou, K. E.; Verykios, X. E. *J. Phys. Chem.* **1993**, *97*, 1184.
- (46) Ohtani, B.; Iwai, K.; Nishimoto, S.-I.; Sato, S. *J. Phys. Chem.* **1997**, *101*, 3350.
- (47) Nozik, A. J.; Memming, R. *J. Phys. Chem.* **1996**, *100*, 13061.
- (48) Gautron, J.; Lemasson, P.; Marucco, J.-F. *Faraday Discuss. Chem. Soc.* **1981**, *70*, 81.
- (49) Mills, A. *J. Chem. Soc., Chem. Commun.* **1982**, 367.
- (50) Hope, G. A.; Bard, A. J. *J. Phys. Chem.* **1983**, *87*, 1979.